

Testing global storm-time electric field models using particle spectra on multiple spacecraft

V. Angelopoulos, M. Temerin, I. Roth, and F. S. Mozer

Space Sciences Laboratory, University of California, Berkeley, California, USA

D. Weimer

Mission Research Corporation, Nashua, New Hampshire, USA

M. R. Hairston

W. B. Hanson Center for Space Sciences, University of Texas, Dallas, Texas, USA

Received 26 March 2001; revised 21 November 2001; accepted 21 November 2001; published 21 August 2002.

[1] During a magnetic storm on 17–18 February 1998, several spacecraft sampled the inner magnetosphere over a wide range of L shells simultaneously and provided a unique opportunity to obtain particle spectra as a function of L shells, latitude, and local time. We present phase space modeling in a dipole magnetic field and with model electric fields during the recovery phase of that storm to explain the ion spectrograms obtained on three spacecraft (POLAR, EQUATOR-S, and FAST). The particle signatures studied are from the late recovery phase of the storm, but the particles are affected by the electric fields along their trajectories also during main phase. Our goal is to test and possibly improve global electric field models, which are crucial to the evolution of the storm-time particle distributions. We backtrace ion distributions from the satellite locations and keep track of charge exchange losses. We use the Volland-Stern, Weimer 96, Weimer 2000, and modifications of Weimer models to best fit instantaneous potential measurements made by the electric field instrument on POLAR and the ion drift meter instrument on the Defense Meteorological Satellite Program fleet of satellites. We incorporate corotation and a simple, global axisymmetric inductive electric field due to the ring current changes. Significant differences with ion spectral observations do exist and cannot be accounted for simply by modification of existing models. Explaining those differences requires addition of local inductive electric fields or nightside injections. *INDEX TERMS:* 2712 Magnetospheric Physics: Electric fields (2411); 2720 Magnetospheric Physics: Energetic particles, trapped; 2753 Magnetospheric Physics: Numerical modeling; 2788 Magnetospheric Physics: Storms and substorms; *KEYWORDS:* storm-time electric fields, storm-time particle distributions, particle tracing, multispacecraft studies, space weather

1. Introduction

[2] In situ dc measurements of electric fields at magnetospheric altitudes have values which vary widely with geomagnetic conditions and typical variances much larger than their means. This makes the global electric field distribution in the magnetosphere a far more elusive quantity than the global magnetic topology (the latter possesses a “ground state” imposed by Earth’s dipole and a quasi-steady global current distribution). Low-altitude satellites have been used in the past to measure the ionospheric potential at the spacecraft location and model it statistically or pass by pass. Under the assumption that the field lines are equipotentials (which is true in the absence of inductive electric fields, when the allowable uncertainty is larger than the field aligned potential drop, i.e., a few kilovolts), the global

electric field can be measured and modeled. Taking advantage of balloon [Mozer *et al.*, 1974] and low-altitude satellite (e.g., S3-3) observations, such modeling has led to global ionospheric electric field patterns [e.g., Heelis *et al.*, 1982] of increasing fidelity. Semi-empirical models like the Volland-Stern model, hereby referred to as the “VS” model, [Volland, 1973; Stern, 1975] were compared and fitted against data for a broad range of geomagnetic activity conditions [Maynard and Chen, 1975]. The availability of the Dynamics Explorer (DE) and the Defense Meteorological Satellite Program (DMSP) data sets have led to more sophisticated models of the average electric potential pattern under a variety of solar wind conditions [Heppner and Maynard, 1987; Rich and Hairston, 1994]. Weimer [1996] presented a generalized data-based model by performing a spherical harmonic representation of the fits to the electric potential averages of DE. This model, herein termed the “W96” model, can compute the ionospheric potential pattern under any interplanetary magnetic field orientation.

More recently, *Weimer* [2001] improved the aforementioned model by incorporating the effects of nightside convection increases under substorm conditions using the *AL* index as an indicator of activity. The improved model is herein termed the “W2k” model. The aforementioned models have been derived from large statistical databases and have not been optimized for storm-time conditions. Observations from Combined Release and Radiation Effects Satellite (CRRES) [*Wygant et al.*, 1998] suggest that storm-time fields penetrate to much lower latitudes in the dusk sector than during nonstorm periods. These low-latitude, storm-time electric fields probably play a key role in populating the innermost *L* shells, but neither their origin nor their effects have been adequately understood because of the lack of electric field measurements in the equatorial inner magnetosphere.

[3] Modeling particle evolution during substorms and storms has been remarkably successful in reproducing gross features of particle distributions in the inner magnetosphere, using the aforementioned simple electric field models and the assumption that the field lines are equipotentials. Specifically, *Ejiri et al.* [1980] were able to model nose dispersions, one of the most dramatic features of substorm and storm time fluxes at the inner magnetosphere at dusk [*Smith and Hoffman*, 1974], using a step function for the electric field increase in a dipole field. “Nose” refers to the shape of the dispersion of a particle enhancement seen in an energy versus *L* shell spectrogram. Particles of energy 10–20 keV make it to low *L* shells at dusk because under a steady electric field those energies correspond to open trajectories and are constantly replenished with particles from the tail. Lower energies correspond to $E \times B$ -dominated closed trajectories and higher energies correspond to gradient/curvature drift dominated closed trajectories, both inaccessible by tail ions. The long residence in such closed trajectories allows losses (such as charge exchange) to deplete fluxes of ions at those energies.

[4] The fact that the ion lifetime is limited in comparison with the residence time on a drift path leads to another interesting feature of the ion spectra. This feature is a decrease of ion flux at a discrete energy (a few keV) seen in energy-time spectrograms in the inner magnetosphere [*McIlwain*, 1972]. The ions of depleted flux are a subset of the ions with open trajectories (accessible from the tail) but simply take a long time to arrive at the satellite location. The energy of lost particles signifies the transition from $E \times B$ -dominated to gradient/curvature drift dominated orbits. *Kistler et al.* [1989], *Fok et al.* [1996], and *Jordanova et al.* [1999] explained observations of storm-time ion spectra on single satellite passes with the above principle. Charge exchange is arguably the dominant loss process. In particular, *Kistler et al.* [1999] compared the particle fluxes obtained from backtracing bounce-averaged particle orbits in a dipole magnetic field and time-dependent models of the electric field. They used the VS and the W96 global electric field models and a dipole magnetic field. The time dependence was obtained from the time dependence of the *Kp* index (for the VS model) or the solar wind parameters (for the W96 model). The resultant fluxes were compared with storm-recovery time observations by the EQUATOR-S satellite, with the objective to determine the electric field model that results in best agreement with the data. The

authors found that of the two electric field models, the W96 model does a better job in reproducing the spectral features of the ions, but that neither model can accurately predict the energies of the observed minima.

[5] It is unclear whether the disagreement between particle tracing under prescribed electric field models and observations is due to the inefficiencies of the electric field models or due to other elements of the procedure (mapping electric potentials to magnetosphere, dipole magnetic field, lack of inductive electric fields). The recent availability of the W2k electric field model with the feature of improved modeling of the nightside ionospheric electric fields as a function of the *AL* index affords us the opportunity to subject this improved model to the same tests as previous models. The improvement is expected to arise from the model’s ability to provide intense nightside electric fields even under northward interplanetary magnetic field (IMF) if the *AL* index shows enhanced activity. Such are the conditions during storm recovery.

[6] We hereby extend the analysis of *Kistler et al.* [1999] on the 17–18 February 1998 storm by incorporating the POLAR and FAST satellite observations. The new data sets present the opportunity to test the same modeling procedure on different local times and a variety of *L* shells. Additionally, we will be testing modified versions of the Weimer electric field models. The modifications are nonlinear fits of the model input parameters to low-altitude satellite data. Finally, we will test the ability of a simple, inductive electric field model to improve the observed spectra. For simplicity, we trace protons, whose particle flux is expected to dominate in late (>8 hours past) storm recovery. Oxygen and other species can also be traced similarly and can be compared with measured energy spectrograms on all three spacecraft. Our objectives are (1) to test the capability of the new electric field models to reproduce the observed particle features, (2) to see how the existing picture for a storm-time ion spectrogram modeling studied by one inner magnetospheric spacecraft (EQUATOR-S) changes by the inclusion of data from two other spacecraft.

[7] In section 2 we describe the general features of the storm and the available data sets. Section 3 deals with the particle tracing procedure, and section 4 deals with the method by which the modified W96 electric field model was derived. In section 5 we discuss the observed spectrograms and present our modeling results.

2. The Event

[8] The storm under study constitutes one of two storms which occurred during the lifetime of the EQUATOR-S satellite [*Haerendel et al.*, 1999]. The availability of EQUATOR-S in an equatorial orbit makes the study of this storm particularly interesting, since the more commonly available off-equatorial spacecraft on other storms provide only a subset of the equatorial phase space density. The simultaneous availability of POLAR and FAST data provides a unique opportunity to study the evolution of particle spectra on a variety of *L* shells and local times. Figure 1 shows the equatorial and ionospheric projections of the three spacecraft, at around 1030 UT. EQUATOR-S was in an inbound orbit at ~ 1000 magnetic local time (MLT) at ~ 1030 UT; POLAR was in the outbound leg of its orbit moving from

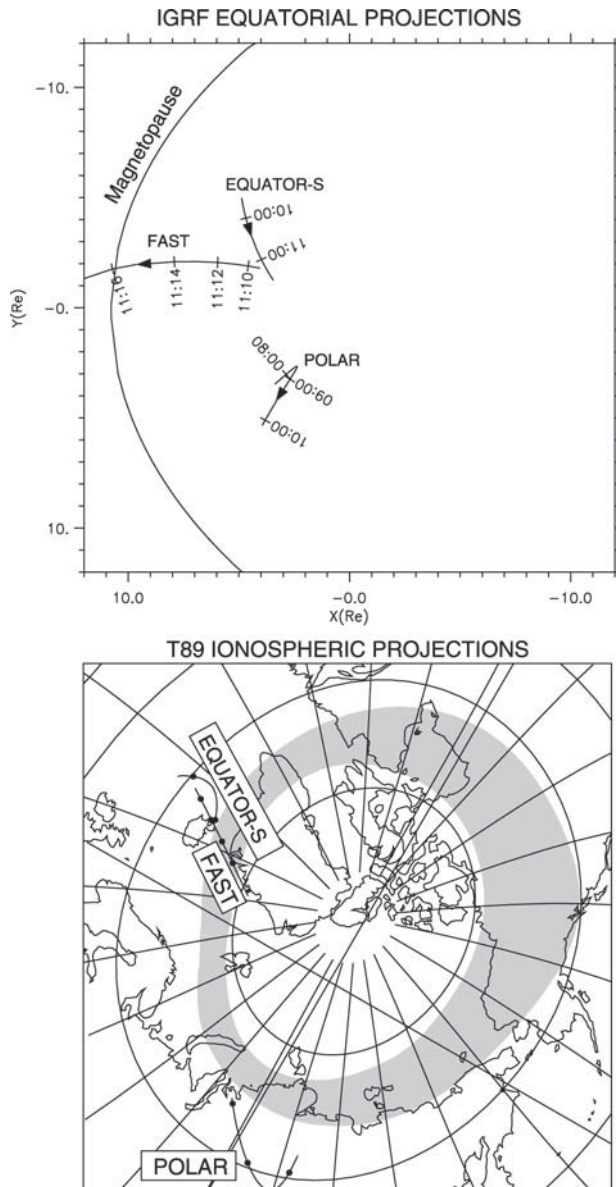


Figure 1. (top) Equatorial projections of spacecraft used to study the 17–18 February 1998 storm. The International Geomagnetic Reference Field model was used for projecting the spacecraft to the magnetic equator. Times are shown in UT and correspond to 18 February 1998. The Sun is to the left. (bottom) Northern ionospheric projections of spacecraft using the *Tsyganenko* [1989] model. Local noon is to the left, and local midnight is to the right. Superimposed on the plot is the corrected geomagnetic coordinate grid at 15° intervals (solid lines) and the geographic coordinate grid at 90° intervals. Also shown by the shaded area is the expected oval position for the measured auroral activity index. The tick marks along the spacecraft projections correspond to the ones in the top figure.

below to above the magnetic equator at ~ 1500 MLT, at ~ 0900 UT; FAST was moving poleward in the northern hemisphere at the dayside approaching the cusp at ~ 1115 UT.

[9] The solar wind data (IMF B_y , B_z , solar wind velocity (V_{sw}) and density (N_{sw})) are shown in Figure 2, advanced in time to Earth's position according to the measured solar wind speed. Also shown are the AL (provisional), Kp , and Dst indices (provisional at 1 min resolution and final at 1 hour resolution) during this storm. The storm main phase started after the southward IMF turning at 1300 UT on 17 February 1998; it lasted for 12 hours. Storm recovery took place from 0000 to 1200 UT on 18 February 1998. The study focuses on the particle spectrograms obtained on the aforementioned spacecraft at the late recovery phase of this storm. However, since the particles are backtraced for 24 hours, the electric field from the entire storm period affects the final particle spectrograms.

3. Tracing Procedure

[10] We followed the motion of particles by integrating the relativistic guiding center equations of motion [Northrop, 1963] in a dipole field geometry and using the electric field prescribed by an ionospheric electric field model. We used the Burlisch-Stoer integration method [Press *et al.*, 1989], and we tested our orbits for consistency against single particle orbits as well as numerically integrated bounce-averaged drift motions in a dipole field. At each step in the integration we derived the VS, W96, W2k model electric field (and their modified versions) at the particle position by mapping analytically the ionospheric electric field along dipole field lines. The VS and W96 models for 89° pitch angle particles backtraced from EQUATOR-S reproduce the same results as those of *Kistler et al.* [1999] but for small differences in the W96 model which have been tracked down to the exact implementation of the time dependence of the electric field model (interpolation/averaging procedure of Kp and of solar wind input). Thus our guiding center particle tracing is also consistent with work of other researchers who integrated the bounce-averaged ion motion. The inductive electric field was computed analytically everywhere from a simple circular line current on the magnetic equator.

[11] Our backtracing starts at a given time and a given satellite's dipole latitude and longitude. In this paper we consider particles locally mirroring at the satellite (though our guiding center code can study any other pitch angle). Backtracing is stopped at a maximum of 24 hours, or until the ions reach an L shell of 10. At each time we keep track of the ratio of the instantaneous particle phase space density to the one at the satellite by updating the particle losses due to charge exchange. This is done, as by *Kistler et al.* [1999], by using the neutral geocoronal model of *Rairden et al.* [1986] and the charge exchange cross section for protons tabulated by *Smith and Bewtra* [1978] for an exobase height of 500 km, an exobase temperature of 1050°K , and a ratio of the critical radius of "satellite" particles [Chamberlain, 1963] to the radius of the exobase of 2.5. If backtracing stops at $L = 10$ (open orbit), then the source phase space density is obtained from a Maxwellian of $T = 20$ keV and $N = 0.1$ cm^{-3} . If backtracing stops at 24 hours (closed orbit), then the source distribution (at $L < 10$) was also derived from a Maxwellian with the same properties as at $L > 10$, but assuming adiabatic transport to the backtracing stopping

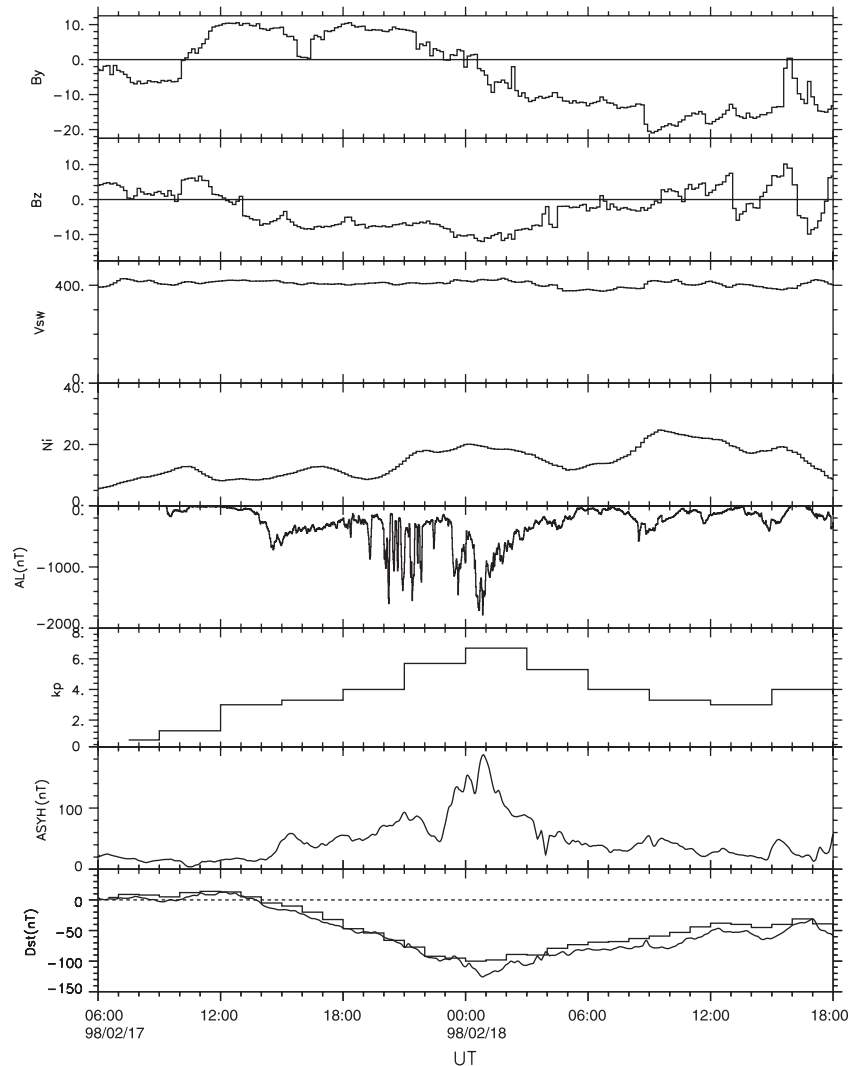


Figure 2. Solar wind parameters from the WIND spacecraft time-shifted according to the measured solar wind speed to correspond to their values at Earth. Also shown are the provisional AL index, the Kp index, the provisional asymmetric H component of the Dst index (1 min resolution), the provisional symmetric Dst index (1 min resolution), which has been corrected for solar wind dynamic pressure effects, and the final Dst index (1 hour resolution).

point. Other source phase space density spatial distributions consistent with FAST storm-time statistical averages, or with CCE typical observations [Kistler *et al.*, 1989] were attempted with similar results. The specifics of our choice of an initial distribution on closed trajectories affects only the depth of the spectral minima, not their position. Our choice of the initial distribution on open trajectories does, however, affect the final particle spectra. The specific choice of temperature and density reflects a visual best match to the data.

[12] Figure 3 shows orbits of different energies (corresponding to different colors) backtraced from the satellite position according to the above methods, using the VS electric field model. While the guiding center bounces up and down the field line, only the field line projection to the magnetic equator is shown here. The top panel corresponds to backtracing from the EQUATOR-S satellite ions of the same energies as in Figure 6a of Kistler *et al.* [1999], in

order to also show the agreement of our guiding center integrator with their bounce-averaged motion integrator, for at least near- 90° pitch angles.

[13] On orbits emanating from all satellites, one feature is evident. As the initial backtraced particle energy increases from below to above ~ 10 keV, the orbits change in character: At low energies the (forward) motion of the particles around Earth is eastward, while at high energies the forward motion is westward. This is because eastward corotation is more important than gradient drifts at low energies, while the westward gradient drifts dominate at higher energies. As described in section 1, particles with intermediate energies spend a long time in the inner magnetosphere. Both the prolonged residence and the high loss rates associated with this motion contribute to rapid loss of phase space density at those energies. Particle spectrograms measured at the satellites show changes in the energy of the phase space density of this primary

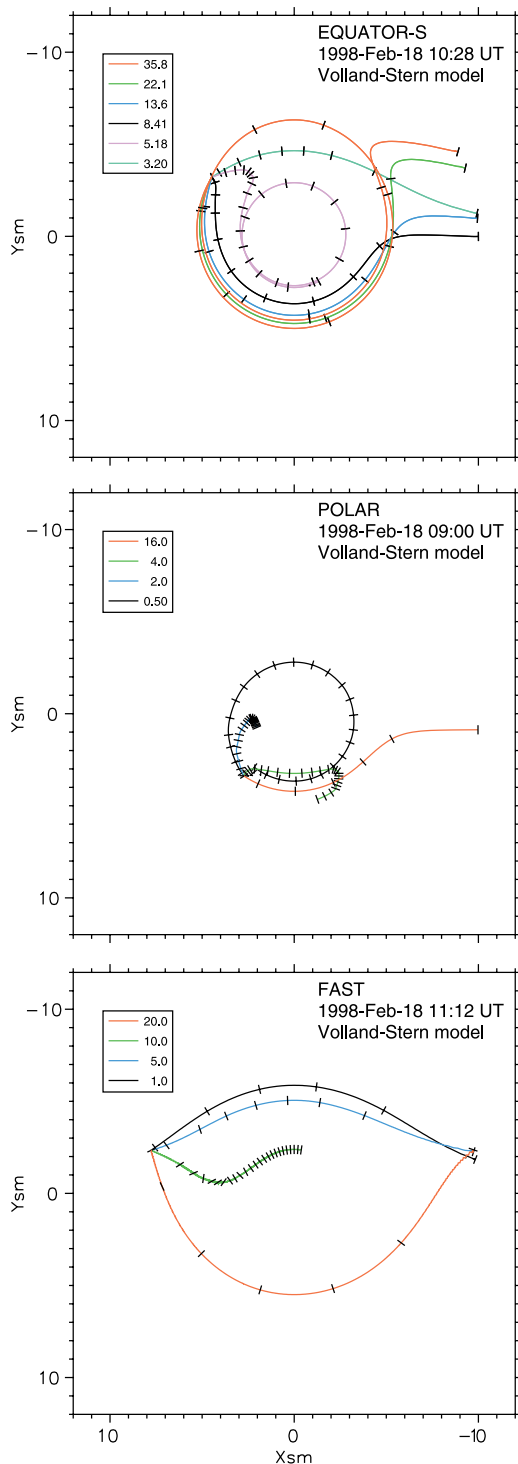


Figure 3. Equatorial projections of guiding center ion motion backtraced from the position of EQUATOR-S, POLAR, and FAST using the VS model for a time-dependent Kp . Tick marks are every hour. The particle's pitch angle at the satellite is 89° and its energy is shown in the insert. The top figure ought to be compared with Figure 6a of Kistler *et al.* [1999].

minimum (and other secondary minima), which we will try to reproduce in this paper using the different electric field models as a means of testing the validity of those models.

4. Electric Field Models

[14] We used dipole mapping to obtain the electric field at any given location from the electric field at the ionosphere as specified by the VS, W96, and W2k models. For the VS model we obtained the 3 hour Kp index, resampled on 1 hour intervals, and then computed the electric field at the position of each particle after linearly interpolating to obtain the instantaneous Kp value. The solar wind values to input in the W96 and W2k models were obtained from 10 min averages in the WIND database projected forward in time to correspond to their values at Earth. The data (IMF B_y , B_z , V_{sw} , and N_{sw}) were linearly interpolated at the times of interest before they entered the W96 or W2k model. Similarly, the AL index (provisional) was obtained at 1 min resolution from the World Data Center and interpolated at the times of interest before usage by the W2k model.

[15] The modified W96 and W2k models (herein referred to as “W96mod” and “W2kmod” models) are improvements of the instantaneous electric field model using available measurements of the polar cap potential by the DMSP and POLAR satellites. The point is that even though the electric field models may not be accurate representations of the global electric field distribution during storms, they can get closer to reality once their input parameters are “tweaked” such that the results match observed traces of the polar cap potential. Toward that goal we used one POLAR pass and many DMSP satellite passes over the auroral zones.

[16] We explain the “W96mod” construction in detail here. Construction of the “W2kmod” was done in an analogous fashion. The POLAR pass occurred over the southern oval (at 0610–0850 UT on 18 February). For that pass we integrated the electric field measured by the electric field instrument [Harvey *et al.*, 1995] along the spacecraft velocity vector to produce the potential along the orbit, assuming the potential was zero at low latitudes ($<55^\circ$). After subtracting the corotation potential, a small potential difference was found between the two 55° latitude points at the two legs of the oval pass (inbound and outbound). The difference was assumed to be due to a small temporal change of the polar cap potential over the ~ 2.5 hour period of the pass. As such, it was subtracted from the trace of the potential by linearly interpolating in time from zero to the full value. The potential thus constructed along the POLAR orbit is shown in Figure 4 (top panel). The bold line in that figure shows the data of the ionospheric potential along the spacecraft track.

[17] Auroral oval crossings by four DMSP satellites (F11, F12, F13, and F14) were also used. The ion drift meter on those satellites provides the ion velocity components perpendicular to the spacecraft motion, which are then used to obtain the potential along the spacecraft track, assuming that the potential is zero at low latitudes. Here, too, the corotation potential was subtracted and the potential offset between the opposite low-latitude points on each pass were assumed to be due to temporal variations and were subtracted after linear interpolation in time. Two such crossings

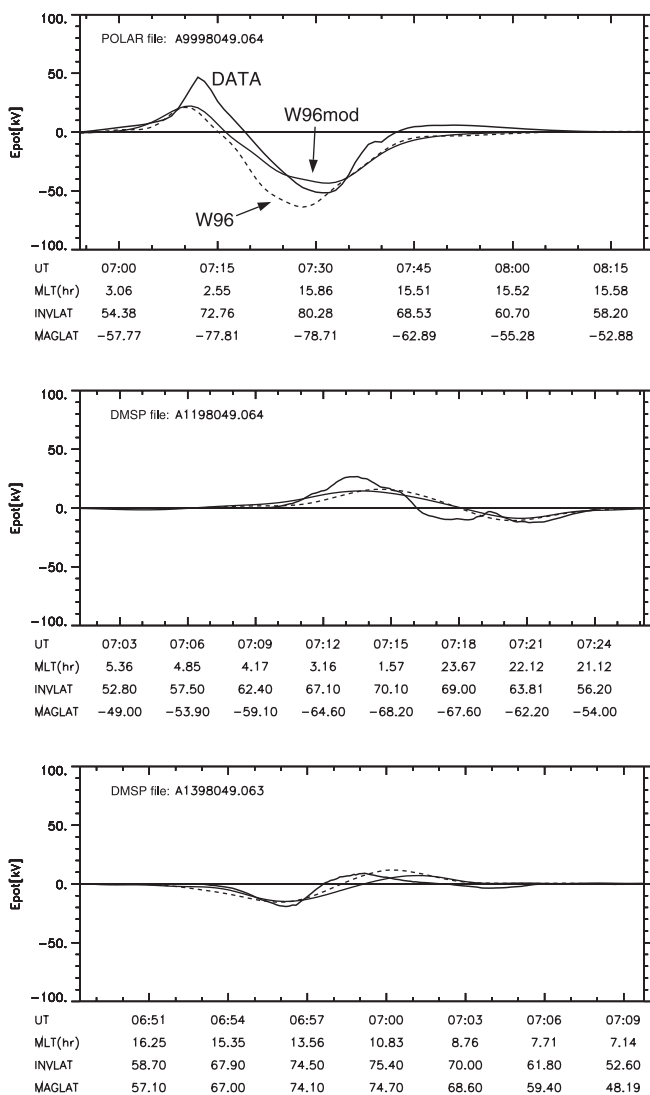


Figure 4. Modeling of ionospheric potential measured by POLAR (top panel) and DMSP (middle and bottom panels) using nonlinear optimization of the Weimer [1996] (W96) model parameters. Bold lines are data; thin dashed lines are W96 model for instantaneous solar wind conditions; thin solid lines are W96mod model, after nonlinear optimization of input parameters to best fit all available ionospheric passes during a 2 hour interval.

by the DMSP F11 (southern oval) and F13 (northern oval) around the time of the POLAR crossing of the southern oval are shown at the bottom two panels of Figure 4 (bold lines). Figure 4 also shows, in thin dashed lines, the W96 values of the potential along the spacecraft track.

[18] Our modeling procedure of the ionospheric data works as follows: The W96 model is a nonlinear function of solar wind parameters (B_y , $B_z \times V_{sw}$). These parameters were varied using the Levenberg-Marquardt method of minimizing the variance with the measured ionospheric potentials obtained on satellites with oval crossings occurring within a 2 hour interval centered at the time of interest. Using the average solar wind values as best guesses, we obtained the best fit W96 parameters as a

function of time, once every 1/2 hour. The nonlinear optimization procedure results in a new set of input parameters to the W96 model, which constitutes the “W96mod” model. The new set of input parameters provides a potential along the satellite tracks that is shown as a thin solid line in Figure 4.

[19] The available DMSP satellites during the 24 hour interval preceding the storm recovery are shown at the bottom panel of Figure 5, while the number of available satellites on each 1/2 hour center is also shown in that figure. All passes were mostly in a dawn-dusk fashion at various distances from the terminator (depending on dipole tilt), providing a relatively good measure of the full potential drop. Our best fit parameters (output from our nonlinear modeling) are shown in Figures 5a, 5b, and 5c as histogram lines. The smooth lines represent the solar wind data (1/2 hour resolution) that were used as best guesses to the fit procedure. Because the W96 model uses the product of B_z and V_{sw} as one parameter, the value of V_{sw} is kept fixed while the value of B_z is allowed to vary. Linearly interpolating in time the 1/2 hour resolution best fit parameters (dashed lines in Figures 5a, 5b, and 5c) allows us to obtain instantaneous values of the electric field at the time and position of interest for particle orbit integrations.

[20] The benefits of using the modified Weimer models arise from the fact that low-latitude electric fields, such as those seen on CRRES during storms [Wygant *et al.*, 1998], if they map to ionospheric altitudes, could actually be modeled by this procedure. Although the VS, W96, and W2k models have been constructed from a large database that would be oblivious to infrequent occurrence of large storm-time electric fields at low latitudes, specific DMSP and POLAR passes during the storm under study would be able to adjust the model to best fit intense low-latitude fields if they are observed at all.

[21] The most current version of the Weimer models, the W2k model, permits a better modeling of the nightside electric fields using the AL index as a proxy of nightside activity and has the additional feature of a variable equatorward oval boundary. Both features make it a tentative improvement for the case of modeling of storm-time fields.

[22] To construct the inductive electric field we used an equatorial, circular line current at radius $a = 2.5-5.5 R_E$. The radius varies linearly with the Dst index to account for the inward motion of the ring current with Dst . The line current intensity was derived analytically as a function of Dst , and the inductive electric field everywhere was computed as a function of the rate of change of Dst . As an example, a 50 nT/hour change in Dst results in a 0.3 mV/m electric field a distance $0.1 R_E$ away from the line current, when the line current is located at $5 R_E$. This is smaller than the corotation electric field at that distance and is thus expected to have a small effect in the particle tracing. The inductive electric field resulting from the modeling of the axisymmetric Dst is 1 order of magnitude smaller than the storm-time electric field observed in the inner magnetosphere by CRRES and reported by Wygant *et al.* [1998]. This modeled inductive electric field is added for completeness to the W2k model and is presented in the following as “W2ki” model, i.e., the Weimer 2000 model with inductive electric fields included. The W2ki model results in ion

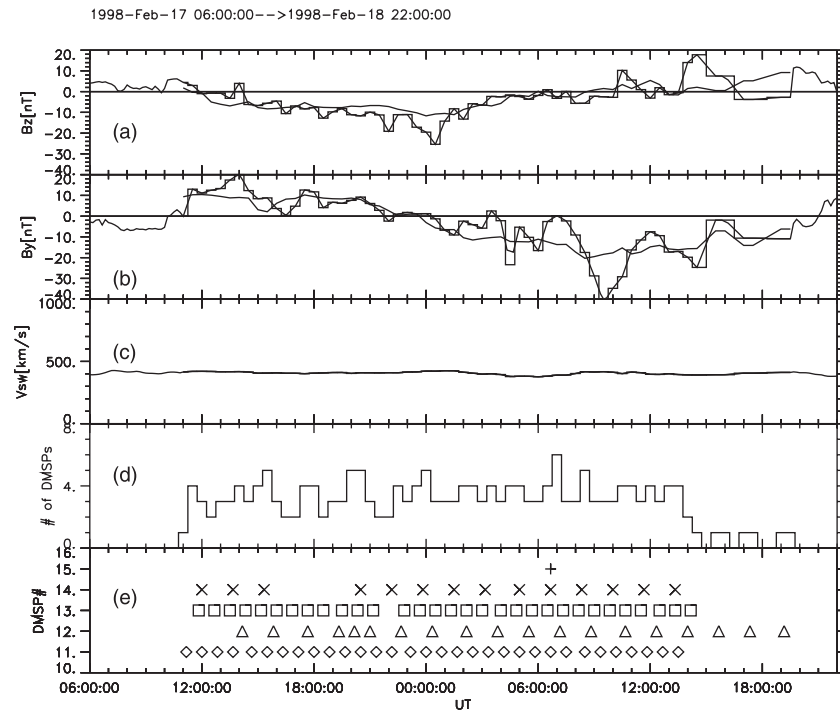


Figure 5. (a, b, c) Solar wind parameters at 1/2 hour resolution. The histogram-mode line shows the results of the nonlinear fit to the Weimer 1996 model for the given ionospheric satellite passes. The solid smooth line shows the data from the WIND spacecraft (same as in Figure 2 but at 1/2 hour resolution) that were used as best guess to the nonlinear fit procedure. (d) Number of spacecraft passes available during a 2 hour interval on each 1/2 hour center. (e) Available passes by DMSP 10–14 and POLAR (indicated as 15). Each symbol represents the beginning time of the ionospheric pass.

spectrograms which are very similar to those of the W2k and W2kmod models.

5. Particle Data

[23] Figure 6 shows, in the bottom row, data from EQUATOR-S, POLAR, and FAST satellites (each column corresponds to a different satellite, with the satellite identified at the top of each column as EQ, PO, and FA). The EQUATOR-S ion spectrogram has been reproduced from Figure 3 of Kistler *et al.* [1999]. The locally mirroring ion (assumed proton) spectra on POLAR were obtained from the HYDRA instrument [Scudder *et al.*, 1995]. On FAST the ion spectrograms were obtained from the ion electrostatic analyzer instrument [Carlson *et al.*, 2001].

[24] EQUATOR-S observed two energy minima (one at ~ 10 keV and another at ~ 4 keV) inside of $L \sim 5.5$. It is evident in the spectrogram that the average energy of both main minima decreases as L shell decreases.

[25] POLAR observed one main minimum at ~ 10 keV. The minimum increased in energy as the satellite moved to smaller L shells and attained its maximum energy at the innermost L shell (0820 UT). The energy of the minimum decreased thereafter, as POLAR moved to the northern hemisphere at higher L shells. A second minimum is observed below the main minimum at 0800 UT. This minimum does not continue as clearly in time (L shell); rather, it becomes a rapid drop in energy flux at energies of 2 keV. A tertiary minimum is seen at ~ 0930 UT at energies of ~ 15 keV, and its energy decreases with time (i.e., L

shell). This minimum might have been present at higher energies at earlier times but would be beyond the energy range of the instrument. Other minima at lower energies are also present at the spectrograms of field-aligned (or field-opposed) particles (not shown) but are not present at 90° pitch angles. Such lower energy-dispersed ion features have been seen also by Freja and other satellites [e.g., Yamauchi *et al.*, 1996] and can be interpreted as nightside injections [Ebihara *et al.*, 2001].

[26] FAST, in the prenoon sector, was approaching the northern cusp when it also observed a major flux minimum at ~ 10 keV, between 1110 and 1116 UT. Lower energy enhancements (< 1 keV) are interpreted as injections, like on POLAR. At 1116 UT, FAST reached the regions adjacent to the cusp and at 1118 UT it entered the cusp, as evidenced by the enhancement of magnetosheath-like (~ 1 keV) plasma population.

6. Results

[27] We trace particle orbits in a dipole field subject to the model electric fields explained above and compute, assuming charge exchange losses, the particle phase space density relative to the phase space density at the source region. This fractional remaining phase space density at the three satellite locations (EQUATOR-S, POLAR, and FAST) is shown in a spectrogram format in Figure 7. Each column corresponds to a different satellite, while each row corresponds to a different electric field model. This format shows features that might otherwise be imperceptible in units of phase

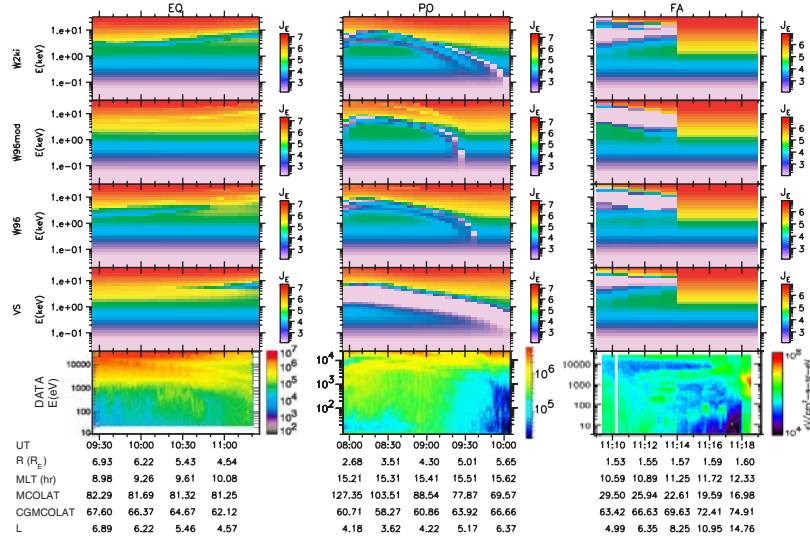


Figure 6. Data (bottom panels) and particle-tracing model-derived (other panels) energy flux spectrograms from EQUATOR-S (EQ, left column), POLAR (PO, middle column), and FAST (FA, right column). The electric field model used in each row is indicated on the left.

space density, such as multiple minima and their evolution in L shell (time).

[28] Using the results of our tracing presented in the four rows of Figure 7, and multiplying them with the

source population at the end of each backtraced orbit, we obtain the upper four rows in Figure 6. As a reminder, the source at $L = 10 R_E$ was an isotropic Maxwellian of $T = 20$ keV and $N = 0.1$ cm $^{-3}$, and at $L < 10$ the source was

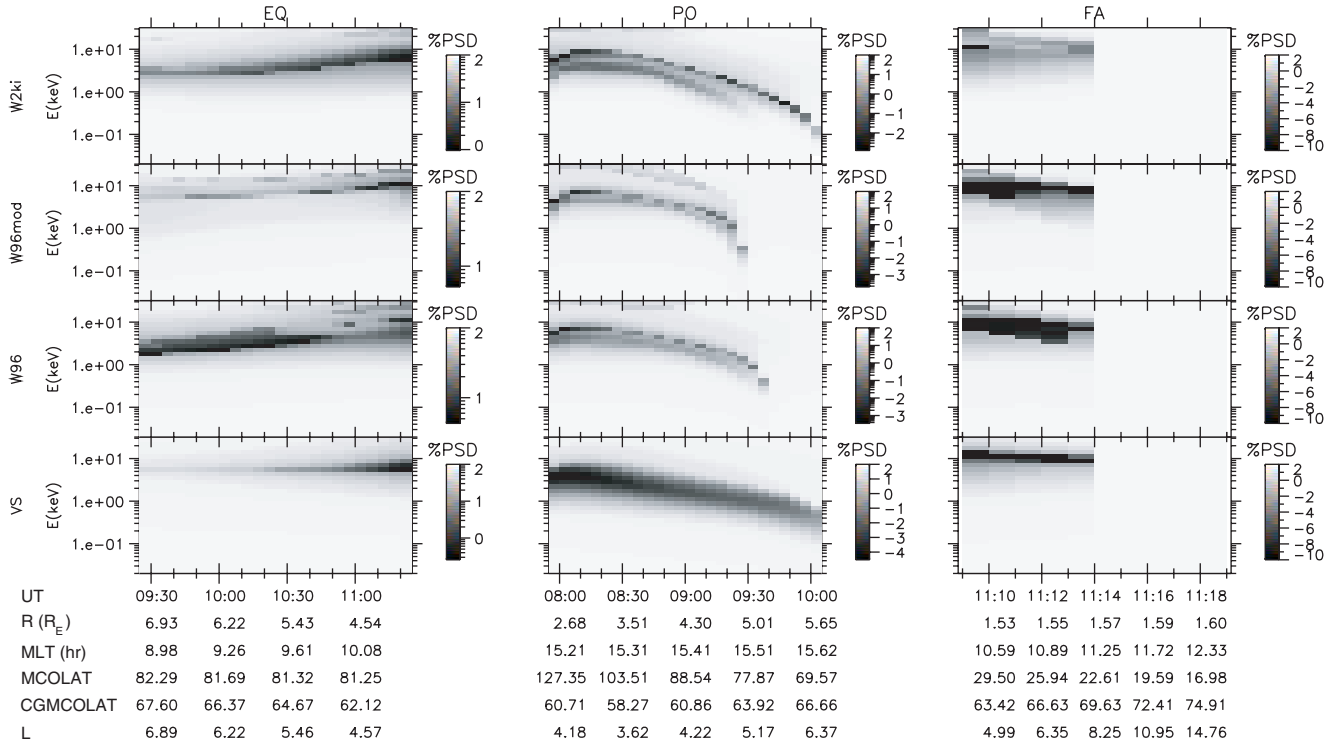


Figure 7. Percent of original phase space density (% PSD) remaining, after charge exchange losses have been incorporated. This times the original phase space density at the point of origin ($L = 10$ or inner magnetosphere if particle is trapped for 24 hours) constitutes the phase space density at the satellite. These panels show clearly the one or more local minima arising primarily from prolonged residence (trapping) at low L shells, where charge exchange losses are also the strongest.

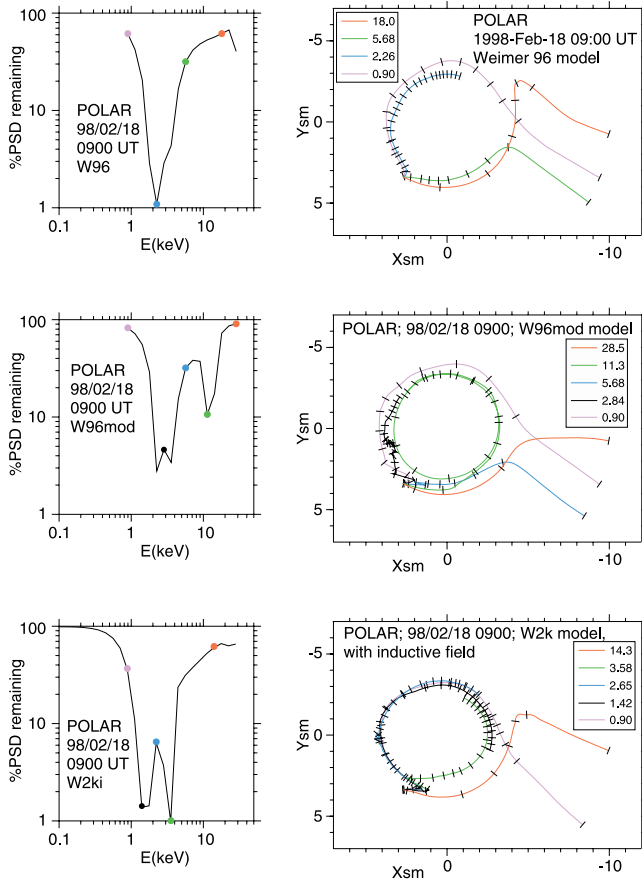


Figure 8. Representative orbits arriving at POLAR, with various energies indicated at the inserts and under the influence of electric field models also indicated at the inserts. On the left of each orbit set are the relative spectra (in units of percent of phase space density remaining after losses through charge exchange), indicating by colored dots the energies of the particles that have been backtraced.

an adiabatically compressed distribution arising from the one at $L = 10$.

[29] Figures 8 and 9 show selective orbits of particles arriving at POLAR at 0930 UT and at EQUATOR-S at 1115 UT, respectively. The orbits were chosen to correspond to local minima or maxima in the relative phase space density. The positions of the minima/maxima are also shown in the same figures as colored dots superimposed on a line spectrogram of the relative phase space density. The line spectrograms correspond to vertical slices of the energy-time spectrograms of Figure 7. With the help of these orbits and the spectrograms of Figures 6 and 7 we will next discuss the salient features of the modeled spectral lines.

[30] All electric field models do an adequate job of predicting the gross features of the main minima (around ~ 10 keV) seen in the measured spectrograms of Figure 6. This is to be expected because the main minimum would result even from a steady dawn-dusk electric field. However, the details of the agreement (or lack thereof) can be quite instructive.

[31] On FAST the 10 keV minimum is reproduced adequately by all electric field models. The sharp change

in the character of the model energy fluxes at 1114 UT is due to the motion of FAST poleward of $L = 10$, which results in immediate assignment of a phase space density consistent with a 20 keV, 0.1cm^{-3} Maxwellian to those points. The FAST data show also a hot magnetospheric-like population prior to entry to the cusp. This layer of hot plasma is thought to come from the tail [Newell and Meng, 1992] due to distortions of the dipole mapping which cannot be accounted for in our model. Thus the success of our model in mapping the observed features past the L shell = 10 is only circumstantial.

[32] On POLAR the modeled fluxes depend significantly on the electric field model chosen. The VS field produces a broad and deep minimum. The W96 model produces more a moderate size minimum (and realistic losses) while both the W96mod and the W2ki models produce a double minimum. The energies of all minima have the correct trend in terms of L shell dependence (peak energy at lowest L shell). However, the minima are at different energies relative to the observed values.

[33] The large breadth and depth of the POLAR minimum arising from the VS model can be understood as follows. Figure 3 shows particle tracing but using the standard (antisymmetric around noon-midnight) VS model. VS equipotentials are small circles at dusk (and dawn). POLAR particles with energies below 2 keV arrive at the satellite from trapped paths at low L shells ($L < 3$), whereas

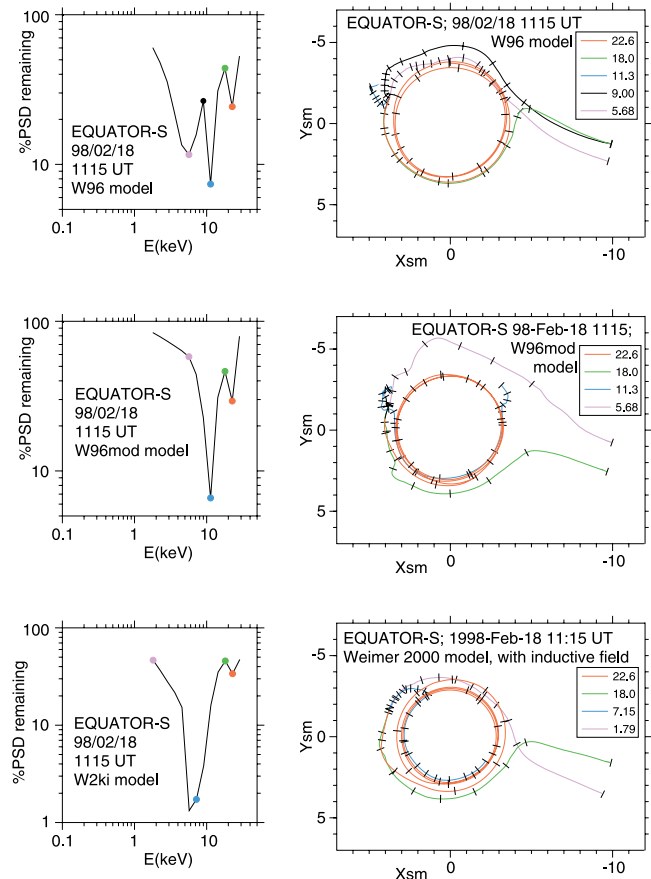


Figure 9. Same as in Figure 8 but for the EQUATOR-S satellite.

in the other models, particles are allowed to come to POLAR from higher L shells, including $L > 10$ (open). This is because the VS equipotentials (i.e., flight paths of low-energy particles) which emanate from POLAR result in particles backtraced closer to Earth, because of the anti-symmetric nature of the VS electric field model. In Figure 8 a 30° counterclockwise asymmetry is introduced to the VS model (resulting in a more realistic ionospheric potential pattern). In that model some of the low-energy particles (below 2 keV) can be replenished from nightside magnetotail fluxes, and the width as well as the depth of the main minimum are reduced. Nevertheless, both the breadth and depth of the POLAR minimum even with the asymmetric VS model are still larger than those of the minima from other models as can be seen in Figure 7.

[34] The double minima occurring when using the W96mod model can be understood in the following fashion: The main minimum at ~ 3 keV (see black dot and black trace in middle panels of Figure 8) occurs because of the $E \times B$ balanced by gradient/curvature drifts. The secondary minimum (see green dot and green trace in middle panels of Figure 8) arises from orbits which have just the right speed to be affected by the large storm-time electric fields 3–4 hours prior to the time of observation. These large fields bring backtraced orbits of those energies closer to Earth and render them trapped orbits. A similar situation occurs when using the W96 model and the W2ki model but for particles of energy greater than ~ 20 keV. These (trapped) orbits are not shown in the respective orbit plots for those models in Figure 8, because they constitute minima of lower significance in those cases.

[35] The double minima resulting from use of the W2ki model can be understood in the following fashion: Orbits of a specific energy get trapped in a stagnation region in the dayside magnetosphere at higher L shells than neighboring energies, i.e., before they have had a chance to convect inward. Thus these orbits are subjected to fewer charge exchange losses than neighboring energies. This creates a sharp local maximum within a broader minimum in relative phase space density. The local maximum is indicated by the blue dot and the blue trace in the bottom panels of Figure 8. The blue backtraced orbit ends at a higher L shell than its neighboring black- and green-colored orbits. It is remarkable that this double minimum is a robust feature in the reconstructed spectrograms of Figure 6. Since the W2ki model reproduces the double minimum seen in the data and the higher-energy tertiary minimum, we conclude that the W2k model does a better job of reproducing the POLAR data than other models.

[36] On EQUATOR-S, use of the W96 model results in a broad minimum, which generally is a poorer reproduction of the observed fluxes (not clearly distinguished in the energy flux spectrogram format). In agreement with the explanation of Kistler *et al.* [1999] the multiple minima from use of the W96 model result from particle trapping in inner L shells due to fortuitous electric field enhancements at the particle flight paths. The minima are not robust in energy or in time. Flight paths corresponding to them can be found in the top panels of Figure 9.

[37] Conversely, use of the W96mod and W2ki models results in robust secondary minima at around 20 keV. These secondary minima are not very clear in the energy flux

spectrogram of Figure 6 but are clearly seen in the relative phase space density spectrograms of Figure 7. As evidenced by the orbits corresponding to those secondary minima in the middle and bottom panels of Figure 9, the minima correspond to trapping of particles in the inner shells due to the intense storm-time electric fields. The position of the secondary minima, however, is (for both model cases) at higher energies (~ 20 keV) than the main minimum, whereas the data show a secondary minimum at lower energies than the main minimum (at ~ 4 keV). While the secondary minimum obtained by our modeling might be seen in the data when plotted in different format, it is clear that it does not represent the physics of the secondary minimum seen at ~ 4 keV. We conclude that no model can reproduce the secondary minimum observed by EQUATOR-S at ~ 4 keV. The position and width of the main minimum (below 10 keV) is reproduced equally well by the VS and W2ki models. However, while in the data both minima decrease in energy with decreasing L shell, all our models show an increase in the energy of the minima with decreasing L shell.

[38] The L shell dependence of the energy of the minima is understood in the following fashion: The energy of the minimum represents the energy where the curvature/gradient drift balances the $E \times B$ drift. A decrease in L shell (which, in a dipole field, results in a decrease in curvature/gradient drift) requires a higher particle energy in order to balance the same $E \times B$ drift. This is a behavior relatively independent of the electric field model used. The data, however, shows a decrease in energy with decreasing L shell. Assuming that the gradient/curvature drifts are modeled accurately enough, this observation suggests that the real $E \times B$ drift decreases with decreasing L shell faster than any model would predict. This is in agreement with the observation of Wygant *et al.* [1998] of reverse sign, intense fields in the inner magnetosphere during storms. Since the storm data-based W96mod model also shows the same behavior as the other models in terms of L shell dependence of the location of the minimum, we conclude that low-altitude observations of electric fields are not sufficient to monitor the magnetospheric electric field. Since low L shells are being considered, the most likely explanation for the discrepancy is the presence of intense inductive electric fields which are expected to be present during storms. The inductive electric field due to the symmetric ring current considered here is too small to account for those phenomena. This electric field peaks during transient Dst fluctuations (at the level of 30–80 nT/hr depending on resolution, see Figure 2) and therefore cannot be the source of the relatively long-lived storm-time electric fields observed on CRRES either.

[39] Since the partial ring current is a current perturbation localized at the evening/premidnight sector, it is a natural source of the inductive electric fields that are required to explain the observations. It is evident from Figure 2 that the asymmetric Dst and its derivative are comparable in magnitude to those of the symmetric Dst index. Therefore the electric field produced from the localized, partial ring current is expected to be much stronger locally than the electric field produced from the symmetric part of the ring current. Those electric fields can be both “forward” and “reverse” according to the sign of the rate of change of the asymmetric ring current.

[40] An alternative explanation of the energy spectrograms may be that the primary ion population indeed

exhibits a primary minimum increasing in energy with decreasing L shell, but superimposed on the spectrogram is the signature of one or more injections with energy decreasing as a function of L shell. The two injections start at energies of 5 and 10 keV at 0930 UT and end at energies 1 and 3 keV, respectively. Modeling of this alternative interpretation of the data would require time-dependent and localized (inductive) electric field enhancement(s) at the nightside. Similar work [e.g., Li *et al.*, 2000] has shown promise that it can explain single satellite spectrograms. If applied in this case, it would have to be consistent with observations on other satellites as well.

7. Conclusions

[41] Statistical storm-time electric field models are difficult to come about because of the scarcity of available data during the limited duration storm periods. Particle tracing in dipole field using model electric fields can be useful in modeling the phase space density expected at various locations in the magnetosphere. Since such modeling depends on the integrated effect of the global electric field along the particle orbit for many hours prior to the observation, such modeling can be a very sensitive and robust test of theoretical or statistical models of storm-time electric fields. We find that while the W2ki model does the best job in reproducing data obtained on the POLAR spacecraft, and all (VS, W96, W96mod, W2k, W2kmod, and W2ki) models can reproduce adequately data obtained on the FAST spacecraft, no model can reproduce well enough the data on the equatorial EQUATOR-S spacecraft. An important clue as to the discrepancy between models and data on EQUATOR-S is the L shell dependence of the energy of the phase space density minimum, which is decreasing with decreasing L shell in the data but has the opposite trend in the models. Inclusion of appropriate localized inductive electric field models is a proposed remedy for this discrepancy. Such fields may be due to localized nightside particle injections or due to storm-time variations of the partial ring current. Our findings also point out the importance of using an equatorial satellite to test the validity of electric field models, since it was the data from such a satellite that resulted in the most significant differences with particle modeling, at least from the perspective of energy spectrograms of locally mirroring particles.

[42] **Acknowledgments.** We wish to thank C. W. Carlson for making the FAST data available and J. Scudder for making the POLAR/HYDRA data available for this study. We are grateful to L. Kistler and J. Bonnell for useful discussions. This work was supported under NASA contract NAS5-30367.

[43] Hiroshi Matsumoto thanks the referees for their assistance in evaluating this paper.

References

Carlson, C. W., et al., The electron and ion plasma experiment for FAST, *Space Sci. Rev.*, **98**, 33, 2001.
 Chamberlain, J. W., Planetary Coronae and atmospheric evaporation, *Planet. Space Sci.*, **11**, 901, 1963.
 Ebihara, Y., M. Yamauchi, H. Nilsson, R. Lundin, and M. Ejiri, Wedge-like dispersion of sub-keV ions in the dayside magnetosphere: Particle simulation and Viking observation, *J. Geophys. Res.*, **106**(A12), 29,571, 2001.
 Ejiri, M., et al., Energetic particle penetrations into the inner magnetosphere, *J. Geophys. Res.*, **85**, 653, 1980.

Fok, M.-C., T. E. Moore, and M. E. Greenspan, Ring current development during storm main phase, *J. Geophys. Res.*, **101**(A7), 15,311, 1996.
 Haerendel, G., R. B. Torbert, and H. Hofner, The Equator-S mission, *Ann. Geophys.*, **17**(12), 1499, 1999.
 Harvey, P., et al., The electric field instrument on the POLAR satellite, *Space Sci. Rev.*, **71**, 583, 1995.
 Heelis, R. A., et al., A model of the high-latitude ionospheric convection pattern, *J. Geophys. Res.*, **87**, 6339, 1982.
 Heppner, J. P., and N. C. Maynard, Empirical high-latitude electric field models, *J. Geophys. Res.*, **92**, 4467, 1987.
 Jordanova, V. K., C. J. Farrugia, J. M. Quinn, R. B. Torbert, J. E. Borovsky, R. E. Sheldon, and W. K. Peterson, Simulations of off-equatorial ring current ion spectra measured by Polar for a moderate storm at solar minimum, *J. Geophys. Res.*, **104**(A1), 429, 1999.
 Kistler, L. M., F. M. Ipavich, D. C. Hamilton, G. Gloeckler, B. Wilken, G. Kremser, and W. Studemann, Energy spectra of the major ion species in the ring current during geomagnetic storms, *J. Geophys. Res.*, **94**(A4), 3579, 1989.
 Kistler, L. M., et al., Testing electric field models using ring current ion energy spectra from the Equator-S ion composition (ESIC) instrument, *Ann. Geophys.*, **17**, 1611, 1999.
 Li, X., et al., Multiple discrete-energy ion features in the inner magnetosphere: Observations and simulations, *Geophys. Res. Lett.*, **27**, 1447, 2000.
 Maynard, N. C., and A. J. Chen, Isolated cold plasma regions: Observations and their relation to possible production mechanisms, *J. Geophys. Res.*, **80**, 1009, 1975.
 McIlwain, C. E., Plasma convection in the vicinity of the geosynchronous orbit, in *Proceedings of a Symposium on Earth's Magnetospheric Processes*, edited by B. M. McCormak, p. 268, D. Reidel, Dordrecht, Netherlands, 1972.
 Mozer, F. S., et al., High-latitude electric fields and the three-dimensional interaction between the interplanetary and terrestrial magnetic fields, *J. Geophys. Res.*, **79**, 56, 1974.
 Newell, P. T., and C. I. Meng, Mapping the dayside ionosphere to the magnetosphere according to particle precipitation characteristics, *Geophys. Res. Lett.*, **19**, 609, 1992.
 Northrop, T. G., *The Adiabatic Motion of Charged Particles*, Wiley-Interscience, New York, 1963.
 Press, W. H., et al., *Numerical Recipes in FORTRAN: The Art of Scientific Computing*, Cambridge Univ. Press, New York, 1989.
 Rairden, R. L., et al., Geocoronal imaging with Dynamics Explorer, *J. Geophys. Res.*, **91**, 13,613, 1986.
 Rich, F. J., and M. Hairston, Large-scale convection patterns observed by DMSP, *J. Geophys. Res.*, **99**, 3827, 1994.
 Scudder, J., et al., HYDRA: A 3-dimensional electron and ion hot plasma instrument for the POLAR spacecraft of the GGS mission, *Space Sci. Rev.*, **71**, 459, 1995.
 Smith, P. H., and R. A. Hoffman, Direct observations in the dusk hours of the characteristics of the storm time ring current particles during the beginning of magnetic storms, *J. Geophys. Res.*, **79**, 966, 1974.
 Smith, P. H., and N. K. Bewtra, Charge exchange lifetimes for ring current ions, *Space Sci. Rev.*, **22**, 301, 1978.
 Stern, D. P., The motion of a proton in the equatorial magnetosphere, *J. Geophys. Res.*, **80**, 595, 1975.
 Tsyganenko, N., A magnetospheric magnetic field model with a warped tail current sheet, *Planet. Space Sci.*, **37**, 5, 1989.
 Volland, H., A semi empirical model of large-scale magnetospheric electric fields, *J. Geophys. Res.*, **78**, 171, 1973.
 Weimer, D. R., A flexible IMF dependent model of high-latitude electric potentials having "space weather" applications, *Geophys. Res. Lett.*, **23**, 2549, 1996.
 Weimer, D. R., An improved model of ionospheric electric potentials including substorm perturbations and application to the Geospace Environment Modeling November 24, 1996, event, *J. Geophys. Res.*, **106**, 407, 2001.
 Wygant, J., D. Rowland, H. J. Singer, M. Temerin, F. Mozer, and M. K. Hudson, Experimental evidence on the role of the large spatial electric field in creating the ring current, *J. Geophys. Res.*, **103**, 29,527, 1998.
 Yamauchi, M., et al., Meso-scale structures of radiation belt/ring current detected by low-energy ions, *Adv. Space Sci.*, **17**, 171, 1996.

V. Angelopoulos, M. Temerin, I. Roth, and F. S. Mozer, Space Sciences Laboratory, University of California, Berkeley, CA 94720, USA. (vassilis@ssl.berkeley.edu)

M. R. Hairston, W. B. Hanson Center for Space Sciences, University of Texas, P.O. Box 830638, MS FO22, 2601 North Floyd Road, Dallas, TX 75083-0688, USA. (hairston@utdallas.edu)

D. Weimer, Mission Research Corporation, 589 West Hollis Street, Suite 201, Nashua, NH 03062, USA. (dweimer@mrcnh.com)